Methane conversion coupled with hydrogen production from water using Au/Ga 2 O 3 photocatalysts prepared by different methods

Article *in* Sustainable Energy & Fuels · January 2023

DOI: 10.1039/D3SE00629H

CITATIONS
2

READS
28

8 authors, including:

Eliane Januario
Serviço Nacional de Aprendizagem Industrial
5 PUBLICATIONS **14** CITATIONS
SEE PROFILE

Saulo Carminati
Instituto de Pesquisas Energéticas e Nucleares
19 PUBLICATIONS **157** CITATIONS
SEE PROFILE

Aryane Tofanello
Universidade Federal do ABC (UFABC)
37 PUBLICATIONS **381** CITATIONS
SEE PROFILE

Bruno Leuzinger Silva
University of Campinas
10 PUBLICATIONS **60** CITATIONS
SEE PROFILE

Sustainable Energy & Fuels

ROYAL SOCIETY OF CHEMISTRY

PAPER

Cite this: *Sustainable Energy Fuels*, 2023, 7, 4288

Methane conversion coupled with hydrogen production from water using Au/Ga_2O_3 photocatalysts prepared by different methods†

Eliane R. Januario, *[a] Saulo A. Carminati, [a] Aryane Tofanello,[b] Bruno L. da Silva,[c] Patricia F. Silvaino,[a] Arthur P. Machado,[a] Jorge M. Vaz[a] and Estevam V. Spinacé[a]

Received 12th May 2023
Accepted 18th July 2023

DOI: 10.1039/d3se00629h

rsc.li/sustainable-energy

Au/Ga_2O_3 photocatalysts were prepared by three different methods (pre-formed Au nanoparticles, borohydride reduction, and impregnation-H_2 reduction) and tested as photocatalysts for methane conversion coupled with hydrogen production from water. The photocatalysts were characterized by X-ray fluorescence, X-ray diffraction, UV-vis, scanning and transmission electron microscopy, X-ray photoelectron spectroscopy, and PL spectroscopy. The reactions were performed with the photocatalysts dispersed in water in a bubbling methane stream under UV-light illumination. The products were identified and quantified by gas chromatography (GC-FID/TCD/MSD). The main products formed were H_2, C_2H_6, CO, and CO_2 with minor quantities of C_2H_4, C_3H_8, and C_4H_{10}. The best performances were observed for the photocatalysts prepared with the nominal Au content of 0.1 wt% regardless of the method used. A production rate of about 100 μmol g^{-1} h^{-1} for C_2H_6 and 15 000 μmol g^{-1} h^{-1} for H_2 was obtained. The Au content, nanoparticle sizes and interactions with Ga_2O_3 strongly influenced the photocatalytic activity.

1 Introduction

Methane (CH_4) is a major constituent of natural gas and is an important carbon and hydrogen source for the chemical industry. However, due to its high stability, it requires high reaction temperatures to convert it into more valuable chemicals. Breaking the C–H bonds of CH_4 requires an energy input of 104 kcal mol^{-1}, and its high symmetry makes activation challenging.[1,2] Steam reforming of methane (SRM) ($CH_4 + 2H_2O \rightarrow 4H_2 + CO_2$) is the main process of methane conversion into hydrogen, and this reaction occurs over the temperature range of 970–1000 K and pressures up to 3.5 MPa.[3] With the demand for a decrease in the use of non-renewable energy, the use of solar energy would be a new stimulus for its replacement.[4,5]

Hydrogen has been highlighted as a possible source of clean energy in the energy transition. Currently, the main applications of hydrogen include oil refining (33%), ammonia production (27%), methanol production (11%), and steel production (3%).[6] The possibility of green hydrogen production technologies is booming because the potential uses of hydrogen are expanding in several areas of research, including power generation,[7] fuel cells for light electric vehicles, heavy transport, and production of green ammonia for fertilizers.[8,9]

A possible method to convert methane into hydrogen and other valuable products at milder temperatures and under milder conditions involves photocatalytic reactions. In this process, a semiconductor is used as a photocatalyst and a source of photoenergy is required to excite an electron (e^-) from the valence band (VB) to the conduction band (CB), creating a vacancy (h^+) in the former. The sites can act as centers for oxidation and reduction reactions (half reactions), respectively. These generated species can participate in oxidation and reduction half-reactions.[10,11] Several photocatalytic methane conversions have been investigated *e.g.*, steam reforming, partial oxidation to oxygenates, and oxidative and non-oxidative coupling of methane[12] where TiO_2,[13–15] ZnO,[16,17] WO_3,[18,19] and Ga_2O_3.[20,21] are the most used semiconductors.

Gallium oxide (Ga_2O_3) has different structures designated as α-, β-, γ-, δ-, and ε-, and these polymorphs are different in terms of crystalline space group order and the coordination number of Ga ions, among which the structure β-Ga_2O_3 is the most thermally stable.[22] β-gallium oxide is a semiconductor with a wide band gap energy (4.8 eV), with its valence band potential located at −7.75 eV and the conduction band potential at −2.95 eV. In

[a]*Instituto de Pesquisas Energéticas e Nucleares, IPEN/CNEN, Av. Prof. Lineu Prestes, 2242-Cidade Universitária, São Paulo, 05508-000, Brazil. E-mail: espinace@ipen.br; eliane.quimica@gmail.com*

[b]*Center for Natural and Human Sciences (CCNH), Federal University of ABC (UFABC), Santo André, 09210-580, SP, Brazil*

[c]*Laboratório de Nanotecnologia e Energia Solar, Instituto de Química, Universidade Estadual de Campinas, Campinas, 13083-970, SP, Brazil*

† Electronic supplementary information (ESI) available: Diffractograms and TEM images of Au/TiO_2 and Au/ZnO, survey spectra of Au/Ga_2O_3 materials, and product chromatograms and formation profile for the photocatalytic reaction. See DOI: https://doi.org/10.1039/d3se00629h

comparison to benchmark TiO_2 (3.2 eV), the photogenerated holes and electrons formed in bulk Ga_2O_3 have stronger redox capacity than those formed in TiO_2. These properties induce the oxidation and mineralization of stable intermediates upon the surface of β-Ga_2O_3.[23] Their properties have attracted increasing interest in methane photooxidation into products.[10,24–26] Recently, Amano and Ishimaru[26] investigated the effect of metal nanoparticles (Au, Ag, Ru, Rh, Pd, and Pt) supported on Ga_2O_3 on the photocatalytic dehydrogenative coupling of methane in the presence of water vapor under UV irradiation. It was observed that the C_2H_6 production in the presence of water vapor was more than 2 orders of magnitude higher than that of conventional photo non-oxidative coupling of methane (in the absence of water). They assumed that CH_4 was activated by $^{\bullet}OH$ radicals, forming $^{\bullet}CH_3$ radicals which, when coupled, form C_2H_6. Among the photocatalysts tested, the Au/Ga_2O_3 photocatalyst was the most effective for C_2H_6 formation.

Li and collaborators[27,28] reported a cooperative photocatalytic system combining the evolution of hydrogen from water and methane conversion. Pt and Pd nanoparticles supported on TiO_2 were used as photocatalysts under UV irradiation producing H_2, C_2H_6, and CO_2 as the main products with minor quantities of C_2H_4 and CO. In this cooperative system, the photo-induced electrons were used for hydrogen production, and the holes for methane conversion. When this process was carried out using only the TiO_2 semiconductor as a photocatalyst, practically no methane conversion or hydrogen production was observed while the conversion of methane and hydrogen production increased with the increase in Pt or Pd loading on TiO_2 reaching a maximum yield around 1.0 to 1.5 wt%. It was also observed that when the reaction was performed in the presence of methane and water the production of hydrogen is two times greater than when it is performed only in the presence of water. Thus, the addition of Pt or Pd nanoparticles on TiO_2 in the presence of methane and water in the reaction medium was shown to be essential to improve the production of ethane and hydrogen. The Pd/TiO_2 photocatalyst was shown to be more selective for ethane production than the Pt/TiO_2 photocatalyst, while the latter was more active for hydrogen production. Although these results are very interesting, the study of other photocatalysts in this cooperative system has been lacking. In this work, Au nanoparticles supported on Ga_2O_3 were synthesized by different methods and their performance as photocatalysts in this cooperative photocatalytic system was investigated.

2 Experimental

2.1 Materials and methods

All materials were used without any previous treatment: tetrachloroauric(III) acid ($HAuCl_4 \cdot XH_2O$, 99.995% purity, Sigma-Aldrich®), gallium oxide (β-Ga_2O_3, ≥99.99% trace metals basis, Sigma-Aldrich®), titanium dioxide (TiO_2 P25 Evonik), zinc oxide (ZnO 100 nm, ~80% Zn basis, Sigma-Aldrich®) sodium borohydride ($NaBH_4$, 98%, Sigma-Aldrich®), sodium citrate tribasic dihydrate ($HOC(COONa)(CH_2COONa)_2 \cdot 2H_2O$, and Sigma-Aldrich®) deionized water (18.2 MΩ cm Milli Q).

2.1.1 Synthesis of Au/Ga_2O_3 photocatalysts. The Au/Ga_2O_3 photocatalysts were prepared with 0.1, 0.5 and 1.0 wt% of Au content by the following methods:

2.1.1.1 Pre-formed Au nanoparticles (PF). The required amounts of a tetrachloroauric acid ($HAuCl_4$) solution (28.88×10^{-3} mol L^{-1}) and sodium citrate solution (92.22×10^{-3} mol L^{-1}) were added (citrate : Au molar ratio of 3) to 64.3 mL of deionized water under stirring. After this, a $NaBH_4$ solution (2.64×10^{-1} mol^{-1} L^{-1}) was added (BH_4 : Au molar ratio of 6) under vigorous stirring and the obtained red solution containing Au pre-formed nanoparticles remained under stirring for 10 min. Then, the required amount of Ga_2O_3 (Sigma-Aldrich) was added and the mixture was maintained under stirring for 24 h. Finally, the solid was separated by centrifugation, washed with excess water and dried at 70 °C. For comparative study, Au/TiO_2 and Au/ZnO (1% wt Au) were synthesized using the same methodology.

2.1.1.2 Borohydride reduction (BH). In this methodology, the Au precursor was reduced using $NaBH_4$ in the presence of Ga_2O_3. First, the required amount of Ga_2O_3 was dispersed in 64.3 mL of water under stirring. After this, the required amount of tetrachloroauric acid ($HAuCl_4$) solution (2.88×10^{-2} mol L^{-1}) was added and the mixture remained under stirring for 10 min. Then, $NaBH_4$ solution (2.643×10^{-1} mol L^{-1}) was added (Au : BH_4 molar ratio of 6) and the resulting mixture remained under stirring for 2 h. Finally, the solid was separated by centrifugation, washed with excess water and dried at 70 °C.

2.1.1.3 Impregnation-H_2 reduction (H_2). Appropriate amounts of tetrachloroauric acid ($HAuCl_4$) solution (2.88×10^{-2} mol L^{-1}) were added to Ga_2O_3. The obtained wet solids were dried, ground and reduced at 200 °C (5 °C min^{-1}) under hydrogen flow (60 mL min^{-1}).

2.2 Characterization

The Au content (wt%) was determined by wavelength-dispersive X-ray fluorescence (WD-XRF) spectroscopy on Rigaku Supermini equipment (Pd source, 50 kV–4 mA) using a calibration curve.

X-ray diffraction (XRD) patterns were recorded on a Rigaku Miniflex II apparatus employing a Cu Kα source ($\lambda = 1.54$ Å) with scanning at 2θ from 20° to 90° with 0.05 step and 2 s count.

UV-Vis spectra were obtained using a Varian UV-Vis spectrometer model Cary 50 from 350 to 700 nm, using $BaSO_4$ as a blank. The optical bandgap (E_g) of the Au/Ga_2O_3 materials was calculated using the Tauc relationship: $\alpha h\nu = (h\nu - E_g)^n$, where α is the absorption coefficient, h is the Planck constant, ν is the frequency and $h\nu$ is the incident photon energy whereas n is the exponent that determines the type of electronic transition causing the absorption. For Au/Ga_2O_3, we considered the indirect allowed transition ($n = 1/2$).

Scanning electron microscopy with field emission gun (SEM-FEG) images were collected on a JEOL equipment model JSM-6701F, coupled with an EDS detector. The samples were dispersed in isopropyl alcohol and deposited onto a sample holder.

Transmission electron microscopy (TEM) images were collected on a JEOL equipment model JEM 2100F, operating at

a voltage of 200 kV. The samples were dispersed in isopropyl alcohol, sonicated for 10 min, and deposited on TEM copper grids. The Au nanoparticle sizes were measured individually to construct the histograms.

X-ray photoelectron spectroscopy (XPS) analyses were performed on a K alpha XPS (Thermo Scientific). Survey spectra were measured (*i.e.*, full range) to identify the elemental composition of materials. High-resolution spectra of Ga_2O_3 and Au nanoparticles were acquired to determine the oxidation state of the elements. The data were analyzed using Thermo Avantage software.

Photoluminescence spectroscopy (PL) was performed with an Ocean Optics 2000 luminescence spectrometer + USB spectrometer with a CCD camera. The excitation wavelength was 265 nm, the photoluminescence spectra were recorded over the range of 250–800 nm, the scanning speed was 1000 nm min^{-1}, and the PMT voltage was 650 V.

2.3 Photocatalytic activity

The reactions were performed in a commercial 250 mL Ace photocatalytic reactor equipped with a Hg lamp (450 W, UV/A/B/C). A steady stream of methane gas (25 mL min^{-1}) was bubbled into 250 mL of water containing 75 mg of the photocatalyst in suspension. A water circulation system was used for cooling the Hg lamp (40 °C) and, in this way, the reactions were carried out at a temperature close to 60 °C. The products were identified by GC-MS (gas chromatography-mass spectrometry) and quantified by GC-FID/TCD on an Agilent 7890B coupled to MSD 5977B equipment, which has a thermal conductivity detector (TCD), methanizer (MET) and flame ionization detector (FID) besides a quadrupole mass spectrometer detector (MSD). Two different columns were used to separate the reaction products, a plot U and a molecular sieve 5 Å column. Twelve injections were performed in a total of 7 h of analysis, each one of 33 min. The first three injections took place with the light switched off, while injections 4 to 10 with the light switched on and in the last two injections the light was turned off again, so it was possible to monitor the influence of light on the system. Calibration curves were constructed to quantify CO, CO_2, C_2H_4, C_2H_6, C_3H_8, C_4H_{10}, and H_2.

3 Results and discussion

The Au content (wt%), particle sizes and bandgap of Au/Ga_2O_3 photocatalysts are shown in Table 1.

In the PF methodology, the Au precursor was reduced by sodium borohydride in the presence of sodium citrate as a stabilizing agent, resulting in a red solution containing Au nanoparticles in the range of 3–5 nm.[29] After this, the Ga_2O_3 semiconductor was then added to this solution to obtain the Au/Ga_2O_3 photocatalyst. However, it was visually observed that not all Au nanoparticles were deposited on the Ga_2O_3 support even after 24 h of stirring. The WD-XRF analyses confirmed that not all the Au nanoparticles were deposited reaching the maximum value of 0.1 wt%, which could be attributed to the surface charge properties of Au nanoparticles and the Ga_2O_3 semiconductor.[30] For comparative purposes, Au/TiO_2 and Au/ZnO with 1.0 wt% of Au content were also prepared using this methodology, and in these cases, the entire Au content was deposited on these supports. In the BH methodology, the Au precursor was reduced by sodium borohydride in the presence of Ga_2O_3 and, in this case, the Au content determined by WD-XRF was very close to the nominal values. Similar results were observed for the H_2 methodology, where the Au precursor was impregnated on the support and reduced in a hydrogen atmosphere.

The X-ray diffractograms of the Au/Ga_2O_3 photocatalysts are shown in Fig. 1.

The diffractogram of the Ga_2O_3 support exhibited peaks consistent with the base-centered monoclinic structure in space group *C*2/*m* (JCPDS: 41-1103). No differences in profile between pure Ga_2O_3 and Au/Ga_2O_3 photocatalysts can be observed. No peaks of $Au^{(0)}$ having a face-centered cubic structure (FCC) at 2θ = 38.1°, 44.3° and 64.5° were observed in the diffractograms,

Table 1 Au content (wt%), particle sizes and bandgap of Au/Ga_2O_3 photocatalysts prepared by different methods

Photocatalyst	Au-WD-XRF (wt%)	Size-TEM (nm)	SD (nm)	Bandgap (eV)
Ga_2O_3 Aldrich	—	—	—	4.6
Au/Ga_2O_3 1.0 wt% PF	0.12	4.6	1.6	4.5
Au/Ga_2O_3 0.5 wt% PF	0.08	4.0	1.4	4.5
Au/Ga_2O_3 0.1 wt% PF	0.03	5.6	2.8	4.6
Au/Ga_2O_3 1.0 wt% BH	0.83	5.1	2.6	4.4
Au/Ga_2O_3 0.5 wt% BH	0.52	4.1	2.5	4.5
Au/Ga_2O_3 0.1 wt% BH	0.10	3.3	0.1	4.4
Au/Ga_2O_3 1.0 wt% H_2	0.95	327	89	4.4
Au/Ga_2O_3 0.5 wt% H_2	0.46	232	76	4.5
Au/Ga_2O_3 0.1 wt% H_2	0.06	29	11	4.5
TiO_2 P25	—	—	—	3.1
Au/TiO_2 1.0 wt% PF[a]	1.03	5.2	1.2	3.0
ZnO 100 nm	—	—	—	3.3
Au/ZnO 1.0 wt% PF[a]	1.03	5.0	1.4	3.3

[a] For comparative purposes.

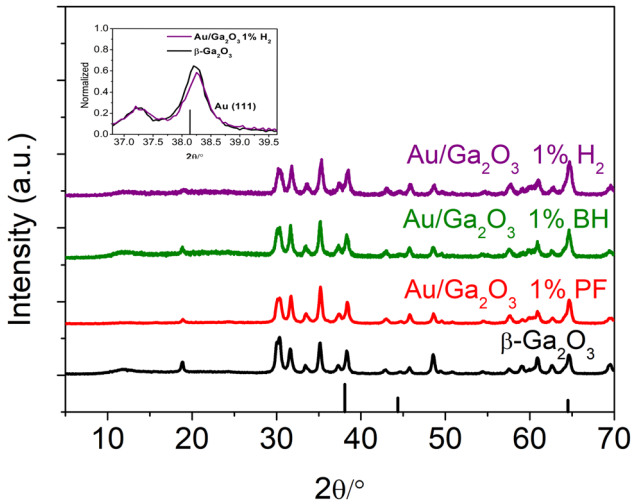

Fig. 1 X-ray diffractograms of the Ga_2O_3 support (black line) and the photocatalysts prepared by different methods with a nominal 1.0 wt% of Au content. The inset shows a zoomed-in image of the Au(111) peak region of Ga_2O_3 and Au/Ga_2O_3 1.0 wt% H_2.

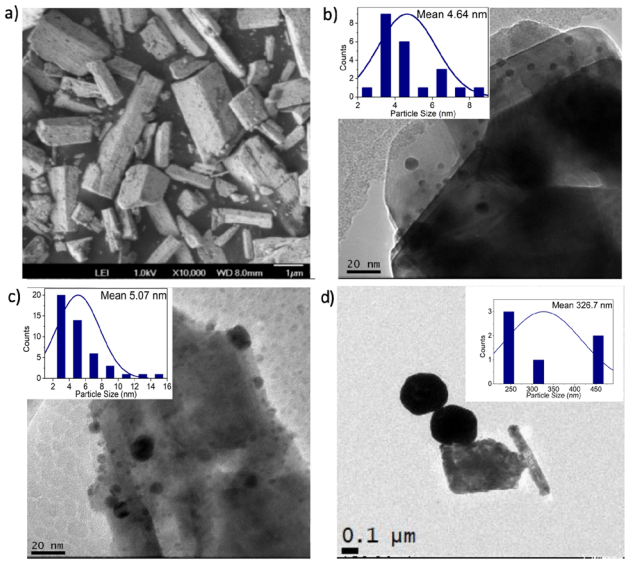

Fig. 2 FEG-SEM micrograph of (a) commercial β-Ga_2O_3 and TEM micrographs with histograms of Au/Ga_2O_3 1.0 wt% photocatalysts (b) PF, (c) BH and (d) H_2.

which could be due to the low content of Au or to the small average nanoparticle sizes resulting in broad and low intensity peaks. Even for the Au/Ga_2O_3 1.0 wt% H_2 photocatalyst, which presented larger Au nanoparticles, peaks of the Au (FCC) phase were not observed, probably due to the small amount of the metal. Diffractograms of Au/TiO_2 1.0% wt and Au/ZnO 1.0% wt are shown as ESI Fig. S1† and exhibit their respective crystalline structures. No peaks of the Au (FCC) phase were observed in these samples either.

The micrographs of the commercial β-Ga_2O_3 and Au/Ga_2O_3 photocatalysts are shown in Fig. 2. In Fig. 2a, it could be seen that the β-Ga_2O_3 material showed a non-uniform morphology, with some large rectangular parallelepiped-shaped crystals and other small crystals with undefined morphology, ranging in size from 1 to 10 μm. The TEM micrograph of Au/Ga_2O_3 PF (Fig. 2b) reveals a well-dispersed distribution of Au nanoparticles with a mean particle size of 4.6 ± 1.6 nm. For the Au/Ga_2O_3 BH photocatalyst (Fig. 2c), a good dispersion of the Au nanoparticles on the support was also observed; however, the histogram displays a high dispersion of Au nanoparticles between 3 and 15 nm with a mean size of 5.1 ± 2.6 nm.

For Au/Ga_2O_3 H_2 (Fig. 2d), the analysis of the micrographs showed the presence of few and large non-homogeneously dispersed Au nanoparticles, with particle sizes ranging from 200 to 450 nm with a mean size of 5.1 326.7 ± 89.6 nm. This may be associated with the phenomenon known as Ostwald ripening, a mechanism dependent on the heating and growth of nanoparticles.[31]

The HR-TEM micrograph of the Au/Ga_2O_3 PF photocatalyst is shown in Fig. 3a where a good contact between Au nanoparticles and the Ga_2O_3 support could be seen. Fig. 3b shows the inter-planar distance of Au nanoparticles of 0.24 nm corresponding to the (111) inter-planar spacing orientation of Au FCC (JCPDS: 4-784).[32] Fig. 3c shows in detail the inter-planar distance of β-Ga_2O_3 of 0.26 nm corresponding to the (111) inter-planar spacing orientation of β-Ga_2O_3 (JCPDS: 41-1103).[33] The micrographs of Au/TiO_2 1.0% wt and Au/ZnO 1.0 wt% are shown in ESI Fig. S2.† The Au nanoparticles showed a good dispersion over the supports and presented sizes of 5.2 ± 1.2 nm for Au/TiO_2 1.0 wt% and 5.0 ± 1.4 nm for Au/ZnO 1.0 wt%.

Diffuse reflectance UV-vis spectra of the Ga_2O_3 support and Au/Ga_2O_3 photocatalysts are shown in Fig. 4. Commercial β-Ga_2O_3 exhibited broad and intense absorption in the UV region below 270 nm, with an estimated band gap energy of 4.8 eV, which is greater than that of the TiO_2 photocatalyst (3.2 eV).[37–41]

The reported VB potential (−7.75 eV) of Ga_2O_3 is lower than that (−7.41 eV) of TiO_2 (relative to the vacuum energy level) and the CB potential (−2.95 eV) of Ga_2O_3 is higher than that (−4.21 eV) of TiO_2. As a consequence, the photogenerated holes and electrons in Ga_2O_3 possess stronger redox capacity than those formed over TiO_2.[23]

Au/Ga_2O_3 PF and BH photocatalysts spectra exhibited absorption bands in the visible region approximately at 540 nm, which are related to the localized surface plasmon resonance (LSPR) of Au nanoparticles.[34] The maximum absorption values (λ_{max}) are similar for these metallic photocatalysts, as they have comparable nanoparticle sizes within the range of 3–5 nm (Table 1). On the other hand, for Au/Ga_2O_3 H_2 photocatalysts the maximum value of these bands shifts to longer wavelengths with the increase of Au content. This is attributed to the size inhomogeneity and irregular dispersion of Au nanoparticles, which is confirmed using TEM micrographs.

The band gap values obtained from Tauc plots are shown in Table 1. For Ga_2O_3, this value was estimated to be 4.6 eV. This value is consistent with the E_g value equal to 4.6–4.8 eV given in the literature.[35,36] No substantial changes in the band gap values were observed for all Au/Ga_2O_3 photocatalysts.

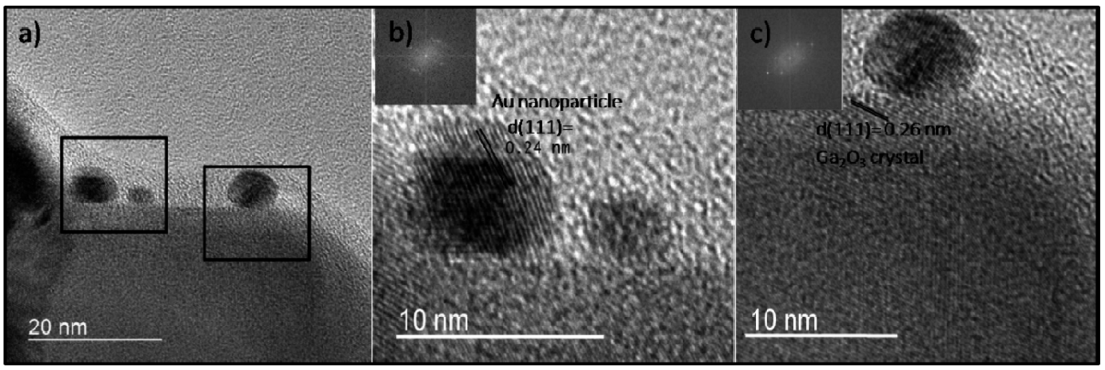

Fig. 3 (a–c) HR-TEM micrographs Au/Ga_2O_3 1.0 wt% PF.

To determine the surface chemical states of β-Ga_2O_3 and Au/Ga_2O_3 photocatalysts, XPS measurements were performed (Fig. 5). All spectra were calibrated using the C 1s peak. The survey spectra (Fig. S3†) showed O 1s, Au 4f, Ga 2p, and Ga 3d binding energies. The Ga 2p region (Fig. 5a) features the expected Ga 2p doublet. The β-Ga_2O_3 material showed a maximum binding energy value at 1117.9 eV for the Ga $2p_{3/2}$ peak and 1145 eV for the Ga $2p_{1/2}$ peak which was attributed to Ga–O bonds in its structure.[37] For Au/Ga_2O_3 photocatalysts these peaks were shifted to higher binding energy values. For instance, for the Ga $2p_{3/2}$ peak, the maximum binding energy values observed were: (1118.48 eV) H_2 > (1118.28 eV) BH > (1118.18 eV) PF > (1117.9 eV) for β-Ga_2O_3. Similar results were described for Pt/TiO_2 catalysts where Ti 2p peaks were shifted to higher binding energies after Pt loading indicating an interaction between Pt nanoparticles and TiO_2.[38]

The Au 4f region of Au/Ga_2O_3 photocatalysts (Fig. 5b) showed two photoemission peaks corresponding to the core-level Au $4f_{7/2}$ and Au $4f_{5/2}$ excitations.[39] For Au nanoparticles, this doublet peak occurs at 83.7 and 87.3 eV, with 3.7 eV corresponding to Au $4f_{7/2}$ and Au $4f_{5/2}$, respectively, typically associated with the presence of Au in the metallic state.[40,41] The Au/Ga_2O_3 photocatalyst synthesized by the PF method showed maximum binding energy peaks at 83.0 and 86.7 eV, and for the material prepared by the BH methodology the values were 83.2 and 86.9 eV and for the material prepared by the H_2 methodology these values were 83.4 and 87.1 eV. Also, for all Au/Ga_2O_3 photocatalysts, these peaks shifted to lower binding energy compared to pure Au nanoparticles.

This behavior is ascribed to a strong metal–support interaction (SMSI) and is indicative of an electron transfer from TiO_2 to Pt.[38,42] Thus, based on these results, it could be also inferred that electrons are transferred from Ga_2O_3 to Au species, and this electronic effect seems to be more pronounced for photocatalysts prepared by PF and BH methods.

From Fig. 5c, it could be seen that the O 1s XPS spectra of β-Ga_2O_3 showed a broad and asymmetric peak centered at 531.0 eV related to O^{2-} species from the oxygen lattice (O_L) with a tail in the region of 532–534 eV attributed to the oxygen (O_2) adsorbed in the vicinity of oxygen vacancies (O_V). The quantity of oxygen adsorbed was correlated with the O_V concentration.[37,43–45] For β-Ga_2O_3, these peaks showed a maximum intensity value at 531.0 and 532.4 eV, respectively. For Au/Ga_2O_3 photocatalysts prepared by PF, BH and H_2 methods, the binding energies were 531.0 and 532.3 eV, 531.0 and 532.5 eV, 531.5 and 532.9 eV, respectively. The O_V/O_L ratio was estimated from peak areas,[45,46] and the value obtained for the β-Ga_2O_3 material was 0.14. For Au/Ga_2O_3 photocatalysts prepared by PF, BH and H_2 methods the values were 0.17, 0.10 and 0.12, respectively. It has been reported that depositing a metal cluster on an oxide surface also favors the formation of oxygen vacancies.[47] Similar results were observed by Wang *et al.*[48] for the prepared Au/CeO_2 by the deposition–precipitation method and they also observed an increase in the O_V/O_L ratio

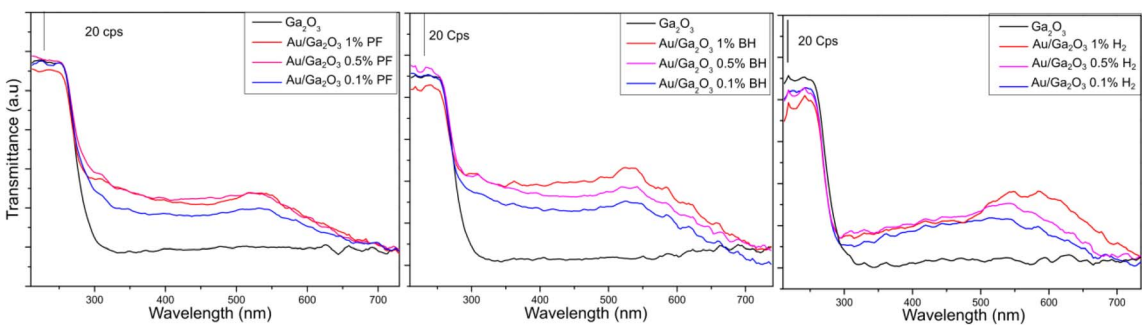

Fig. 4 Diffuse reflectance UV-vis spectra of Ga_2O_3 and Au/Ga_2O_3 photocatalysts.

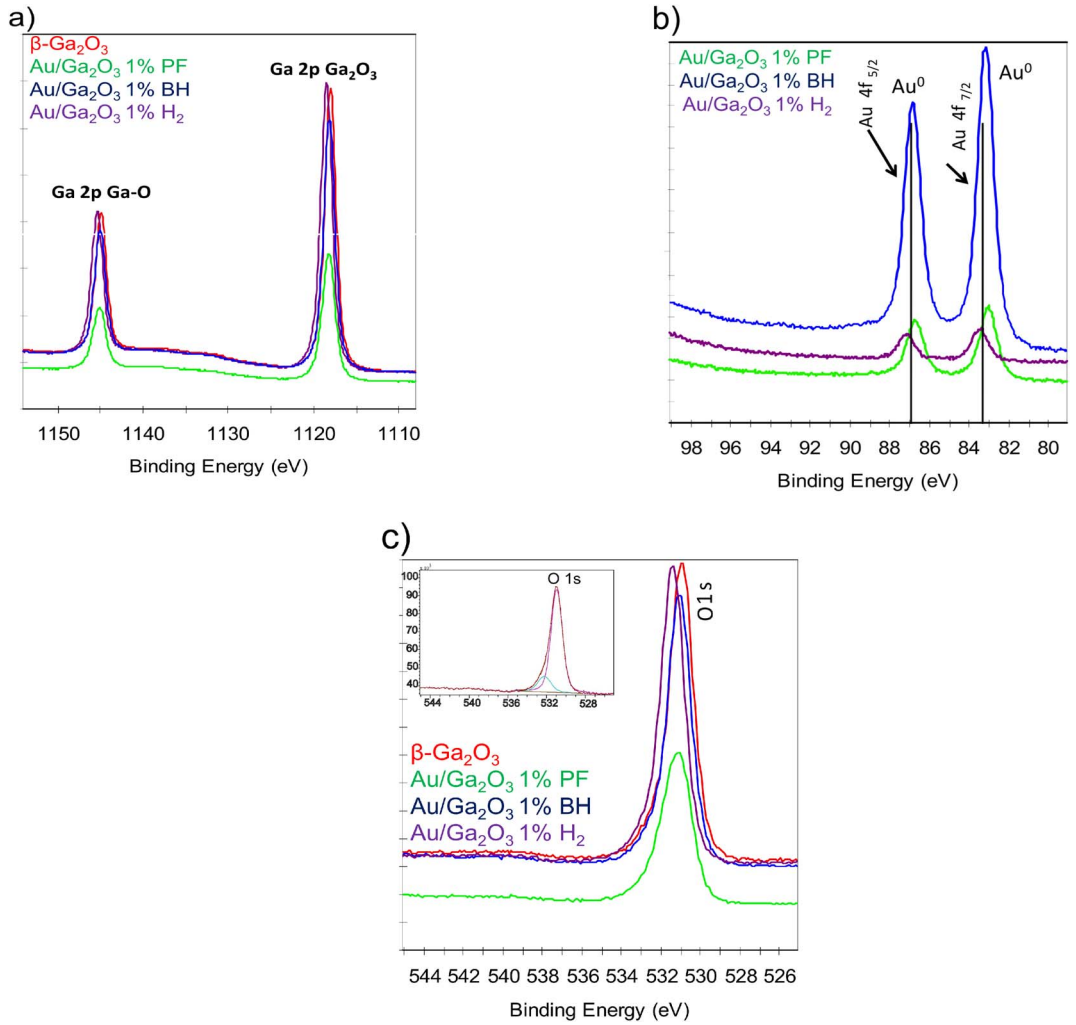

Fig. 5 XPS spectra of Ga_2O_3 and Au/Ga_2O_3 1.0 wt% photocatalysts: (a) Ga 2p region, (b) Au 4f region and (c) O 1s region (inset shows the deconvoluted spectrum of the Au/Ga_2O_3 1.0 wt% PF photocatalyst).

after the deposition of Au nanoparticles on the CeO_2 support. Thus, an increase in oxygen vacancies was only observed for Au/Ga_2O_3 photocatalysts prepared by the PF methodology. Oxygen vacancies can act as electron acceptors promoting the separation of photogenerated charge carriers and enhancing the performance of the photocatalysts.[44]

Fig. 6 shows the PL spectra of commercial β-Ga_2O_3 and Au/Ga_2O_3 photocatalysts.

PL spectroscopy has been used to investigate the electronic interactions between noble metal nanoparticles and semiconductors. It was observed that the deposition of noble metal nanoparticles on TiO_2 resulted in the attenuation of the PL signal of TiO_2 due to a decrease in the recombination of electron–hole pairs.[39] From Fig. 6a, it could be seen that β-Ga_2O_3 showed a PL emission peak centered around 425 nm resulting from the recombination of an electron in an oxygen vacancy or Ga ion center and a hole trapped in a Ga ion vacancy.[49] For the Au/Ga_2O_3 1.0 wt% photocatalyst, the shapes of the emission spectra were very similar to those of β-Ga_2O_3 and a decrease in the intensities for the PL emission peaks at about 425 nm was also observed indicating an improvement of the charge separation for all photocatalysts. On the other hand, the decrease in the PL emission peak was greater for BH and H_2 than for the PF photocatalyst. It should be noted that although these photocatalysts have a nominal Au content of 1.0 wt%, the real Au content of the PF photocatalyst was only 0.1 wt%. It was observed for Au/Ga_2O_3 photocatalysts that the intensity of the PL emission peak decreases with the increase of Au content even though the material has a larger Au nanoparticle size.[50] As shown in Fig. 6b, a clear decrease in the PL emission peak intensities was observed for Au/Ga_2O_3 photocatalysts prepared by the BH method with an increase in Au content.

The photocatalytic activity of commercial β-Ga_2O_3 and Au/Ga_2O_3 photocatalysts for methane conversion coupled with hydrogen production from water is summarized in Table 2. The reactions performed in the absence of a photocatalyst and in the presence of light resulted in only a small amount of CO_2 formation. No products were formed when the reactions were carried out in the absence of light, regardless of the photocatalyst used (ESI, Fig. S4†). Using β-Ga_2O_3 as a photocatalyst,

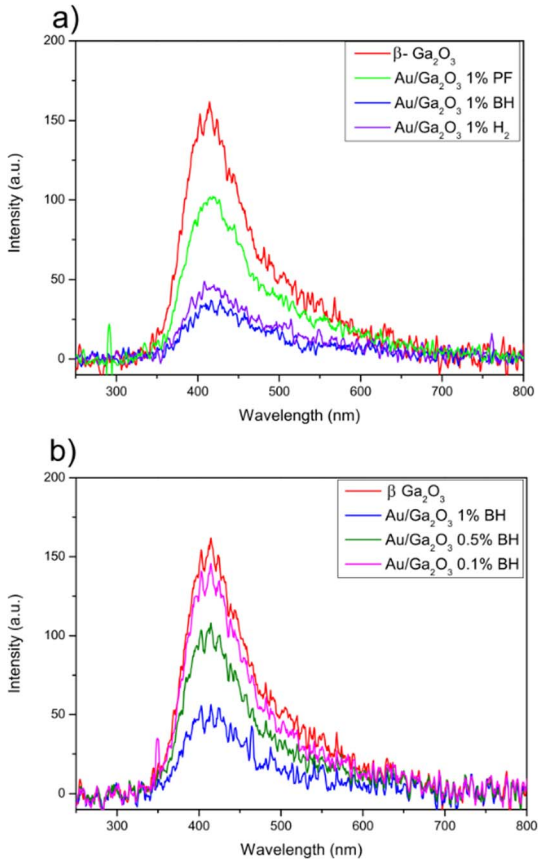

Fig. 6 PL spectra (a) β-Ga_2O_3 and Au/Ga_2O_3 photocatalysts 1.0 wt% prepared by PF, BH and H_2 methods and (b) Au/Ga_2O_3 BH photocatalysts with 0.1, 0.5 and 1.0 wt% Au.

Table 2 Product formation using commercial β-Ga_2O_3 and Au/Ga_2O_3 photocatalysts (75 mg of photocatalyst, 250 mL H_2O, 25 mL min^{-1} CH_4, 450 W Hg lamp)

	Product formation rates (μmol g^{-1} h^{-1})						
Photocatalyst	C_2H_6	C_2H_4	C_3H_8	C_4H_{10}	CO	CO_2	H_2
Without photocatalyst	—	—	—	—	—	9	—
β-Ga_2O_3	73	1	3	—	93	1080	3712
Au/Ga_2O_3 1.0 wt% PF	130	6	14	1	181	4504	12 800
Au/Ga_2O_3 0.5 wt% PF	81	8	8	—	275	5096	16 400
Au/Ga_2O_3 0.1 wt% PF	104	4	13	1	155	4488	15 360
Au/Ga_2O_3 1.0 wt% BH	63	15	14	1	233	2368	7560
Au/Ga_2O_3 0.5 wt% BH	67	20	15	1	322	2920	9920
Au/Ga_2O_3 0.1 wt% BH	100	11	15	1	310	4836	15 070
Au/Ga_2O_3 1.0 wt% H_2	59	2	5	—	81	808	3604
Au/Ga_2O_3 0.5 wt% H_2	58	1	4	—	92	759	3016
Au/Ga_2O_3 0.1 wt% H_2	129	2	8	1	209	3285	10 062
TiO_2 P25	73	—	3	—	25	140	—
Au/TiO_2 1.0 wt% PF[a]	135	5	13	2	37	455	1856
ZnO 100 nm	4	0	1	1	5	85	—
Au/ZnO 1.0 wt% PF[a]	5	1	3	1	6	71	—

[a] For comparative purposes.

the formation of appreciable amounts of H_2, CO_2, CO, and C_2H_6 was observed. A chromatogram is shown in ESI Fig. S5.† In the presence of Au/Ga_2O_3 PF photocatalysts, it was observed that the amounts of products formed were very similar for all photocatalysts as these materials have very similar chemical compositions (about 0.1 wt% of Au) despite being initially prepared with different nominal Au contents (Table 1).

The H_2 and CO_2 production rates increased about fivefold when compared to β-Ga_2O_3 while the increase of CO and C_2H_6 production rates was about twice. For these photocatalysts, it was also observed that the formation of small quantities of C_2H_4, C_3H_8 and C_4H_{10}. Au/Ga_2O_3 BH photocatalysts achieved increased performance, which was observed to be inversely proportional to the amount of Au, that is, the material with the lowest amount of Au (0.1 wt%) was more active. Curiously, for this photocatalyst the product formation rates were very similar to those of Au/Ga_2O_3 PF photocatalysts, which contain similar Au contents. It was already observed that there was an optimal quantity of metal loading to prepare metal/semiconductor photocatalysts and that an increase of it may cause a decrease in the performance probably contributing to the recombination process of charge carriers instead of promoting charge separation.[51]

Au/Ga_2O_3 H_2 photocatalysts prepared with Au content of 0.5 and 1.0 wt% showed production rates very similar to that of β-Ga_2O_3, which is probably due to the great sizes of Au nanoparticles (in the range of 200 to 300 nm) present in these materials. On the other hand, the Au/Ga_2O_3 H_2 photocatalyst prepared with Au content of 0.1 wt%, which has Au nanoparticles with an average size of about 30 nm, showed an increase in the activity compared to β-Ga_2O_3, but the production rates were lower than those obtained for photocatalysts prepared by PF and BH methods with equivalent amounts of Au but with Au nanoparticle sizes in the range of 3–5 nm. For comparative purposes, Au/TiO_2 and Au/ZnO 1.0 wt% PF photocatalysts were also tested, showing inferior performance to the Au/Ga_2O_3 1.0 wt% PF photocatalyst. Similar results were recently reported by Amano and Ishimaru[26] for photocatalytic dehydrogenative coupling of methane in the presence of water vapor using Au/Ga_2O_3 photocatalysts with Au content of 0.1 and 0.5 wt%. The products formed were CO_2, CO, C_2H_6 and H_2 and the photocatalyst with Au content of 0.1 wt% also showed superior performance. They also observed that the activity was greatly influenced by Au nanoparticle sizes and it was suggested that Au–Ga_2O_3 interfaces promote water oxidation by holes producing $^{\bullet}OH$ radicals that react with CH_4 to produce $^{\bullet}CH_3$ that coupled forming C_2H_6 since no adsorption of CH_4 on Au/Ga_2O_3 photocatalysts was observed by FTIR analysis. Li *et al.*[27,28] also reported that in the presence of water and CH_4 using metal/TiO_2 as photocatalysts, the $^{\bullet}OH$ radical was the species that dehydrogenated CH_4 forming the $^{\bullet}CH_3$ radical that coupled to form C_2H_6.

4 Conclusions

Au/Ga_2O_3 photocatalysts were shown to be active for methane conversion coupled with hydrogen production from water under mild conditions. The main products formed were H_2, CO_2, CO and C_2H_6 with minor quantities of C_2H_4, C_3H_8 and C_4H_{10}. TEM and UV-Vis analysis showed that Au/Ga_2O_3 photocatalysts prepared by PF and BH methods have smaller Au nanoparticle sizes than the photocatalysts prepared by the H_2 method. XPS

analysis of Ga 2p and Au 4f regions of Au/Ga_2O_3 photocatalysts indicate the presence of $Au^{(0)}$ and Ga–O species from the β-Ga_2O_3 structure for all photocatalysts, and furthermore, the photocatalysts prepared by PF and BH methods exhibited a more pronounced interaction between Au nanoparticles and Ga_2O_3 that could result in electron charge transfer from Ga species to Au. The O 1s XPS spectra suggest an increase in oxygen vacancies only for the Au/Ga_2O_3 photocatalyst prepared by the PF method. PL emission spectra showed a decrease in intensities for the emission peaks for all Au/Ga_2O_3 photocatalysts when compared to β-Ga_2O_3 suggesting a decrease in the recombination of electron–hole pairs. The Au/Ga_2O_3 photocatalysts with Au content of 0.1 wt% showed better performance than the materials with Au content of 0.5 and 1.0 wt% for all methods used. Au/Ga_2O_3 photocatalysts prepared by PF and BH methods showed superior performance and this could be attributed to smaller Au nanoparticle sizes and their interactions with the β-Ga_2O_3 structure.

Author contributions

E. R. J. performed the catalyst synthesis, characterization, photocatalytic tests, and writing. S. A. C. and A. T. collaborated in analyses, and discussion of results. B. L. S. participated in the photoluminescence experiments and discussion. P. S. F. and A. P. M. participated in the catalyst preparation, characterization and photocatalytic tests of Au/TiO_2 1.0 wt% and Au/ZnO 1.0 wt%, respectively. J. M. V. and E. V. S. designed the study and reviewed the paper. All authors have read and agreed to the published version of the manuscript.

Conflicts of interest

There are no conflicts to declare.

Acknowledgements

The authors gratefully acknowledge support from São Paulo Research Foundation (FAPESP – grant numbers 2017/11937-4, 2018/04596-9, 2018/04595-2, and 2021/01896-4), Brazilian National Council for Scientific Development (CNPq – Grant numbers 305622/2020-0 and 407967/2022-2) and Shell and the strategic importance of the support given by ANP (Brazilian National Oil, Natural Gas and Biofuels Agency) through R&D levy regulation. We also acknowledge the support given by Prof. Ana Flávia Nogueira from "Laboratório de Nanotecnologia e Energia Solar", Chemistry Institute, UNICAMP for providing the facilities of photoluminescence experiments and LNNano for XPS measurements (proposal no. 20221012) and TEM (proposal no. 20210567).

References

1 N. S. N. Hasnan, S. N. Timmiati, K. L. Lim, Z. Yaakob, N. H. N. Kamaruddin and L. P. Teh, *Mater. Renew. Sustain. Energy*, 2020, **9**, 1–18.
2 K. Harun, S. Adhikari and H. Jahromi, *RSC Adv.*, 2020, **10**, 40882–40893.
3 E. R. Januario, P. F. Silvaino, A. P. Machado, J. Moreira Vaz and E. V. Spinace, *Front. Chem.*, 2021, **9**, 1–11.
4 K. Shimura, S. Kato, T. Yoshida, H. Itoh, T. Hattori and H. Yoshida, *J. Phys. Chem. C*, 2010, **114**, 3493–3503.
5 X. Du, Z. Yang, X. Yang, Q. Zhang, L. Liu and J. Ye, *Energy Fuels*, 2022, **36**, 3929–3937.
6 H. H. Cho, V. Strezov and T. J. Evans, *SSRN Electron. J.*, 2022, **8**, 13585–13595.
7 M. Otto, K. L. Chagoya, R. G. Blair, S. M. Hick and J. S. Kapat, *J. Energy Storage*, 2022, **55**, 105714.
8 F. Yilmaz and M. Ozturk, *Int. J. Hydrogen Energy*, 2022, **47**, 31911–31926.
9 H. Zhou, Y. Ma, Q. Yang, D. Wang, H. Li, G. Li, Y. Yang, Z. Fan, D. Ji, N. Li and D. Zhang, *J. Cleaner Prod.*, 2022, **362**, 132445.
10 L. Yuliati, T. Hattori, H. Itoh and H. Yoshida, *J. Catal.*, 2008, **257**, 396–402.
11 K. Takanabe, *J. Catal.*, 2019, **370**, 480–484.
12 Z. Chen, S. Wu, J. Ma, S. Mine, T. Toyao, M. Matsuoka, L. Wang and J. Zhang, *Angew. Chem., Int. Ed.*, 2021, **60**, 11901–11909.
13 J. Xie, R. Jin, A. Li, Y. Bi, Q. Ruan, Y. Deng, Y. Zhang, S. Yao, G. Sankar, D. Ma and J. Tang, *Nat. Catal.*, 2018, **1**, 889–896.
14 C. Mateos-Pedrero, S. R. González-Carrazán, M. A. Soria and P. Ruíz, *Catal. Today*, 2013, **203**, 158–162.
15 H. Song, X. Meng, S. Wang, W. Zhou, S. Song, T. Kako and J. Ye, *ACS Catal.*, 2020, **10**(23), 14318–14326.
16 Z. Li, X. Pan and Z. Yi, *J. Mater. Chem. A*, 2019, **7**, 469–475.
17 H. Song, X. Meng, S. Wang, W. Zhou, X. Wang, T. Kako and J. Ye, *J. Am. Chem. Soc.*, 2019, **141**, 20507–20515.
18 K. Villa, S. Murcia-López, T. Andreu and J. R. Morante, *Appl. Catal., B*, 2015, **163**, 150–155.
19 J. Yang, J. Hao, J. Wei, J. Dai and Y. Li, *Fuel*, 2020, **266**, 117104.
20 M. Ishimaru, F. Amano, C. Akamoto and S. Yamazoe, *J. Catal.*, 2021, **397**, 192–200.
21 S. P. Singh, A. Anzai, S. Kawaharasaki, A. Yamamoto and H. Yoshida, *Catal. Today*, 2021, **375**, 264–272.
22 S. I. Stepanov, V. I. Nikolaev, V. E. Bougrov and A. E. Romanov, *Rev. Adv. Mater. Sci.*, 2016, **44**, 63–86.
23 J. Wei, J. Yang, Z. Wen, J. Dai, Y. Li and B. Yao, *RSC Adv.*, 2017, **7**, 37508–37521.
24 J. Wei, J. Yang, Z. Wen, J. Dai, Y. Li and B. Yao, *RSC Adv.*, 2017, **7**, 37508–37521.
25 K. Shimura, T. Yoshida and H. Yoshida, *J. Phys. Chem. C*, 2010, **114**, 11466–11474.
26 F. Amano and M. Ishimaru, *Energy Fuels*, 2022, **36**, 5393–5402.
27 L. Yu, Y. Shao and D. Li, *Appl. Catal., B*, 2017, **204**, 216–223.
28 L. Yu and D. Li, *Catal. Sci. Technol.*, 2017, **7**, 635–640.
29 C. S. L. Alencar, A. R. N. Paiva, J. C. M. Da Silva, J. M. Vaz and E. V. Spinace, *Mater. Res.*, 2020, **23**, 2–7.
30 Z. Xia, V. Rozyyev, A. U. Mane, J. W. Elam and S. B. Darling, *Langmuir*, 2021, **37**, 11618–11624.
31 T. Akita, P. Lu, S. Ichikawa, K. Tanaka and M. Haruta, *Surf. Interface Anal.*, 2001, **31**, 73–78.

32 R. Torres-Mendieta, D. Ventura-Espinosa, S. Sabater, J. Lancis, G. Mínguez-Vega and J. A. Mata, *Sci. Rep.*, 2016, **6**, 1–9.
33 J. Cooke, L. Ghadbeigi, R. Sun, A. Bhattacharyya, Y. Wang, M. A. Scarpulla, S. Krishnamoorthy and B. Sensale-Rodriguez, *Phys. Status Solidi A*, 2020, **217**, 1–9.
34 K. W. Choi, D. Y. Kim, X. L. Zhong, Z. Y. Li, S. H. Im and O. O. Park, *CrystEngComm*, 2013, **15**, 252–258.
35 B. Alhalaili, R. J. Bunk, H. Mao, H. Cansizoglu, R. Vidu, J. Woodall and M. S. Islam, *Sci. Rep.*, 2020, **10**, 1–14.
36 Y. Kawaguchi, M. Yamamoto, A. Ozawa, Y. Kato and T. Yoshida, *Surf. Interface Anal.*, 2019, **51**, 79–84.
37 A. Trinchi, S. Kaciulis, L. Pandolfi, M. K. Ghantasala, Y. X. Li, W. Wlodarski, S. Viticoli, E. Comini and G. Sberveglieri, *Sens. Actuators, B*, 2004, **103**, 129–135.
38 M. Y. Byun, Y. E. Kim, J. H. Baek, J. Jae and M. S. Lee, *RSC Adv.*, 2022, **12**, 860–868.
39 Y. Chen, Y. Wang, W. Li, Q. Yang, Q. Hou, L. Wei, L. Liu, F. Huang and M. Ju, *Appl. Catal., B*, 2017, **210**, 352–367.
40 P. Jiang, S. Xie, J. Yao, S. He, H. Zhang, D. Shi, S. Pang and H. Gao, *Chin. Sci. Bull.*, 2001, **46**, 996–998.
41 Y. Chen, Y. Wang, W. Li, Q. Yang, Q. Hou, L. Wei, L. Liu, F. Huang and M. Ju, *Appl. Catal., B*, 2017, **210**, 352–367.
42 H. Iida and A. Igarashi, *Appl. Catal., A*, 2006, **298**, 152–160.
43 C. V. Ramana, S. Roy, V. Zade, A. K. Battu, N. Makeswaran and V. Shutthanandan, *J. Phys. Chem. Solids*, 2021, **157**, 110174.
44 J. Liu, W. Lu, Q. Zhong, H. Wu, Y. Li, L. Li and Z. Wang, *J. Colloid Interface Sci.*, 2018, **519**, 255–262.
45 Y. Yang, S. Zhao, F. Bi, J. Chen, Y. Li, L. Cui, J. Xu and X. Zhang, *Cell Rep. Phys. Sci.*, 2022, **3**, 101011.
46 H. Tang, Z. A. Chen, C. Ouyang, Z. Ye, S. Li, Z. Hong and M. Zhi, *J. Phys. Chem. C*, 2022, **126**, 20036–20048.
47 A. R. Puigdollers, P. Schlexer, S. Tosoni and G. Pacchioni, *ACS Catal.*, 2017, **7**, 6493–6513.
48 X. Wang, B. Chen, G. Chen and X. Sun, *RSC Adv.*, 2016, **6**, 87978–87987.
49 S. R. Meitei and N. K. Singh, *Appl. Phys. A: Mater. Sci. Process.*, 2019, **125**, 1–6.
50 J. Lu, J. Xing, D. Chen, H. Xu, X. Han and D. Li, *J. Mater. Sci.*, 2019, **54**, 6530–6541.
51 W. H. Lin, Y. H. Chiu, P. W. Shao and Y. J. Hsu, *ACS Appl. Mater. Interfaces*, 2016, **8**, 32754–32763.